



1 **Measurement report: Characteristics of airborne black**
2 **carbon-containing particles during the 2021 summer**
3 **COVID-19 lockdown in Yangzhou, China**

4

5 Yuan Dai^{1,2,3}, Junfeng Wang^{1,2}, Houjun Wang³, Shijie Cui^{1,2}, Yunjiang Zhang^{1,2},

6 Haiwei Li^{1,2}, Yun Wu^{1,2}, Ming Wang^{1,2}, Eleonora Aruffo⁵, Xinlei Ge^{1,2,4*}

7

8 ¹Jiangsu Key Laboratory of Atmospheric Environment Monitoring and Pollution

9 Control, Collaborative Innovation Center of Atmospheric Environment and Equipment

10 Technology, School of Environmental Science and Engineering, Nanjing University of

11 Information Science and Technology, Nanjing 210044, China

12 ²International Joint Laboratory on Climate and Environment Change (ILCEC), Nanjing

13 University of Information Science and Technology, 210044 Nanjing, China

14 ³Yangzhou Environmental Monitoring Center, Yangzhou 225009, China

15 ⁴School of Environment and Energy Engineering, Anhui Jianzhu University, Hefei

16 230601, China

17 ⁵Department of Advanced Technologies in Medicine & Dentistry, University “G.

18 d’Annunzio” of Chieti-Pescara; Center for Advanced Studies and Technology-CAST,

19 Chieti 66100, Italy

20

21 **Correspondence:** Xinlei Ge (caxinra@163.com)

22



23 **Abstract**

24 Black carbon-containing (BCc) particles are pervasive in ambient atmosphere. The
25 unexpected outbreak of the COVID-19 pandemic in 2021 summer prompted a localized
26 and prolonged lockdown in Yangzhou City, situated in the Yangtze River Delta (YRD)
27 region, China, which provides a unique opportunity to gain insights into the relationship
28 between emission sources and BCc. Satellite and ground-level measurements both
29 demonstrated that strict emission controls effectively reduced local gaseous pollutants.
30 Meanwhile, single particle aerosol mass spectrometer (SPA-MS) analysis showed that
31 the number fraction of freshly emitted BCc particles decreased to 28% during the
32 lockdown (LD), with that from vehicle emissions experiencing the most substantial
33 reduction. However, the uncontrolled reductions of nitrogen oxides (NO_x) and volatile
34 organic compounds (VOCs) likely contributed to increased ozone (O₃) concentrations,
35 increased the oxidizing capacity, which may in turn enhanced secondary PM_{2.5}
36 formation and compensated the primary PM_{2.5} reduction. As a result, we did observe a
37 slight increase of PM_{2.5} concentration (21.2 μg m⁻³) during the LD period compared to
38 the period before the lockdown (BLD), and the increase of more aged BCc particles.
39 Reactive trace gases (e.g., NO_x, SO₂, and VOCs) could form thick coatings on pre-
40 existing particles likely via enhanced heterogeneous hydrolysis under high RH as well,
41 resulting in significant BCc particle growth (~600 nm) during LD period. Furthermore,
42 BCc source apportionment reveals that BCc particles were primarily of local origin
43 (78%) in Yangzhou during normal summertime. However, coal combustion (23%) and
44 vehicle emissions (21%) were prominent non-local pollution sources, with the air mass
45 originating from the southeast, along with biomass burning emissions (19%) from the
46 northeast, contributing significantly. Our research highlights that short-term, strict local
47 emission controls may not effectively reduce PM pollution, due to the non-linear
48 responses of PM_{2.5} to its precursors, further effective PM_{2.5} reduction requires a
49 comprehensive and extensive approach with a regionally coordinated and balanced
50 control strategy through joint regulation.

51

52 **1. Introduction**

53 China has implemented long-term clean air measures to cut down anthropogenic
54 emissions and improve air quality (Ge et al., 2020), resulting in a nationwide reduction
55 of average fine particulate matter (PM_{2.5}, aerodynamic diameter ≤ 2.5 μm) level from
56 50 μg m⁻³ in 2015 to 30 μg m⁻³ in 2020 (Zhou et al., 2022). However, this PM_{2.5}
57 concentration remains significantly higher than the new World Health Organization
58 (WHO) guideline value of 5 μg m⁻³ (WHO *Global Air Quality Guidelines*, 2021). Black
59 carbon (BC) is a ubiquitous component of PM_{2.5} that can mix with various species, and
60 the number fraction of BC-containing particles (BCc) can be higher than 50% of PM_{2.5}
61 in China (Sun et al., 2022; Xie et al., 2020; Chen et al., 2020). Additionally, the
62 atmospheric aging of BCc involves complex chemical and physical processes,
63 influencing their mixing state, morphology, hygroscopic and optical properties, etc.,



64 ultimately impacting their climatic and health effects (Bond et al., 2013; Ramanathan
65 et al., 2008). Reducing the mass loading of BCc is therefore essential to comply with
66 the new WHO PM_{2.5} guideline. Moreover, the insufficient understanding of complex
67 emission sources (e.g., fossil fuel and biomass burning), aging processes (e.g.,
68 coagulation, condensation, and cloud processing), and physical properties (e.g., mixing
69 state and coating composition) of BCc, hampering the effectiveness of air quality
70 remediation (Cappa et al., 2019; Kahnert, 2010; Sun et al., 2021).

71

72 Yangzhou is located in the central region of Yangtze River Delta (YRD), at the junction
73 of the Yangtze River and, the Beijing-Hangzhou Grand Canal, which serves as a
74 prominent economic city, industrial-intensive area, and highly active inland shipping
75 node in East China. Due to the complex emissions and feedback with the East Asian
76 monsoons, this region is susceptible to anthropogenic aerosols, especially BCc particles
77 originating from chemical, steelmaking, coal-fired, petrochemical enterprises, and
78 transportation, etc. Extensive studies have investigated the responses of atmospheric
79 pollutants to emission changes during the COVID-19 lockdown measures in the YRD
80 (Chen et al., 2021; Li et al., 2020; Qin et al., 2021; K. Zhang et al., 2022). However,
81 the key chemical and physical processes specifically responsible for the BCc particles
82 in this region are still not fully understood. During the summer of 2021, Yangzhou
83 experienced a resurgence of COVID-19 with over 500 confirmed cases. In response,
84 stringent public health measures were imposed from July 28th to September 10th,
85 including the closure of public transport, and suspension of non-essential industrial
86 plants, restaurants, shopping malls, and entertainment clubs. People were also
87 mandated to quarantine at home. Unlike the nationwide COVID-19 lockdown in China
88 during the cold season of 2020 (Le et al., 2020; Sulaymon et al., 2021b), the summer
89 lockdown in Yangzhou was more localized but protracted, significantly altering local
90 anthropogenic emissions while neighboring cities maintained regular operations. This
91 scenario provides a unique opportunity to explore and compare the diverse mixing
92 states and aging process of BCc particles in different anthropogenic emission-intensive,
93 investigate the regional transportation of air pollutants in the YRD, enhance our
94 knowledge about the formation of BC-associated secondary components (Lei et al.,
95 2021; Zhang et al., 2020) and understand emissions-meteorology interactions (Jiang et
96 al., 2021; Le et al., 2020) in the YRD.

97

98 Studies on the effects of large-scale and short-term stringent emission control events on
99 air quality in China have been widely deployed, e.g., the 2008 Beijing Olympic Games
100 (Wang et al., 2010; Zhou et al., 2010), the 2015 Asia-Pacific Economic Cooperation
101 (APEC) (Zhu et al., 2015), the 2014 Nanjing Youth Olympic Games (Wang et al., 2022)
102 and the national COVID-19 lockdown in 2020 winter (Huang et al., 2021; Le et al.,
103 2020; Li et al., 2020; Wang et al., 2020). Previous studies extensively investigated air
104 pollutant variations during the COVID-19 lockdown in the winter of 2020 across
105 different regions of the world. Stringent restrictions on industrial and vehicular



106 activities have resulted in significant reductions in gaseous pollutants and particulate
107 matter, not only in megacities (Chen et al., 2020; Jeong et al., 2022; Sun et al., 2020)
108 but also in middle-sized cities (Clemente et al., 2022; Wang et al., 2021; Xu et al., 2020)
109 and rural areas (Cui et al., 2021, 2020; Jain et al., 2021). Compared to the decreasing
110 trends observed in most cities worldwide, the level of PM_{2.5} in Shanghai (Chang et al.,
111 2020), Hohhot (Zhou et al., 2022), and the Northeast of China Plain (Nie et al., 2021)
112 increased unexpectedly. These observations reveal the complex aerosol chemistry of
113 PM_{2.5} comprising primary and secondary components. The reduction of primary
114 pollutants during lockdown resulted in a shift towards a higher proportion of secondary
115 aerosols, including inorganic and organic species, exhibiting a non-linear response to
116 emission changes (Zhang et al., 2021). Furthermore, some studies have suggested that
117 the increase in secondary aerosols during lockdown is due to the enhanced atmospheric
118 oxidative capacity resulting from the rise in ozone levels (Wang et al., 2021),
119 unfavorable meteorological conditions (Chien et al., 2022; Sulaymon et al., 2021a),
120 changes of local and regional emission sources (Feng et al., 2022), etc. However, most
121 previous studies focused on lockdown events during the cold seasons, studies on
122 summer lockdown events in China were very limited.

123

124 To better understand the chemical compositions and aging characteristics of airborne
125 BCc particles in the YRD, we conducted ground measurements, spaceborne
126 observations, and mass spectrometric analysis during the COVID-19 2021 summer
127 lockdown in Yangzhou. Besides, We employed potential source contribution function
128 (PSCF) analysis and a novel approach for distinguishing local sources to study the air
129 pollution regional transport in the YRD. This study investigated the impact of small-
130 scale and short-term stringent emission controls on local ambient aerosol and the
131 mixing state of BCc particles, providing valuable insights for future air pollution control
132 measures.

133

134 **2. Methods**

135 **2.1 Sampling site and instruments**

136 The in-situ online measurements were conducted at a rooftop laboratory 20 m above
137 ground located in a national air quality monitoring station, Yangzhou Environmental
138 Monitoring Center (32.41°N, 119.40°E), Yangzhou, China (Figure 1). This sampling
139 site is a typical urban site surrounded by residential areas, arterial roads, parks,
140 restaurants, and shopping centers. In this study, the measurement period was divided
141 into three phases: the before-lockdown period (BLD: 30 June to 27 July 2021), the
142 lockdown period (LD: 28 July to 9 September 2021), and the after-lockdown period
143 (ALD: 10 September to 7 October 2021) (Figure 2).

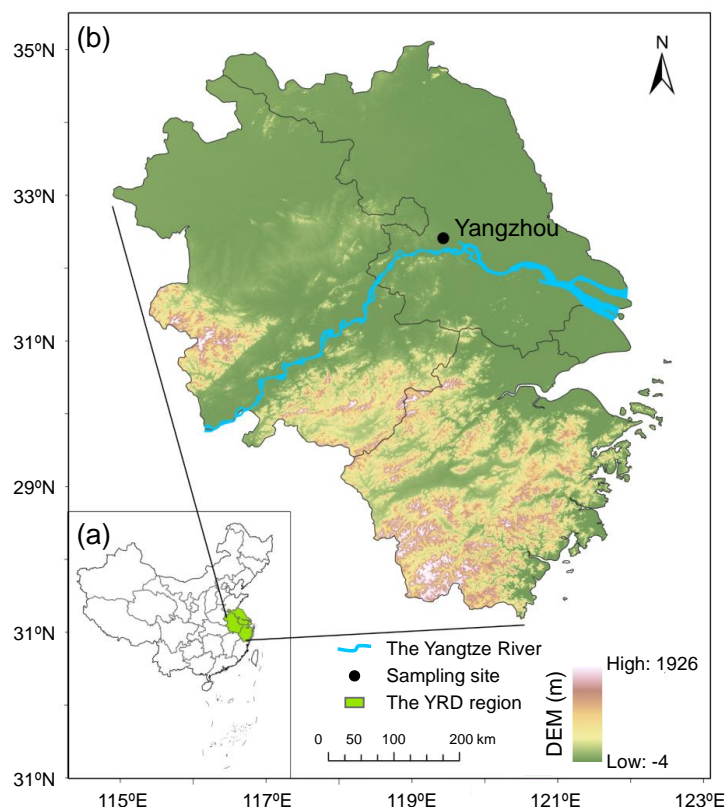
144

145 A single-particle aerosol mass spectrometer (SPA-MS, Hexin Analytical Instrument Co.,
146 Ltd., China) was deployed during the field campaign to obtain chemical composition,



147 size distribution, and mixing state of individual PM_{2.5} particles. A PM_{2.5} cyclone (Model
148 URG-2000-30ED) and a Nafion dryer are equipped in front of the sampling inlet.
149 Individual particles are introduced into the SPA-MS through a critical orifice with a
150 flow rate of 3 L min⁻¹. The vacuum aerodynamic diameters (D_{va}) are determined using
151 the velocities derived from two continuous laser beams (diode Nd: YAG, 532 nm)
152 spaced 6 cm apart. Subsequently, these particles are desorbed and ionized by a
153 downstream pulsed laser (266 nm), and ion fragments are generated and measured by
154 a Z-shaped bipolar time-of-flight mass spectrometer. A more detailed description of
155 SPA-MS can be found in previous studies (Li et al., 2011, Zhang et al., 2022).

156
157 PM_{2.5} mass concentration was measured by a particulate matter monitor (XHPM2000E,
158 Xianhe, China). Nitrogen oxides (NO_x = NO + NO₂), SO₂, and ozone (O₃)
159 concentrations were detected with a set of Thermo Fisher Scientific instruments
160 (Models 42i, 43i, and 49i). The concentrations of 103 volatile organic compounds
161 (VOCs) in ambient air, comprising 57 ozone precursors (PAMS), 12 aldehydes and
162 ketones, and 34 toxic organics (TO15), were continuously monitored at hourly intervals
163 using an online device (TH-300B, Tianhong, China). Meteorological parameters,
164 including ambient temperature (T), relative humidity (RH), precipitation (PCP), wind
165 direction (WD), and wind speed (WS) were observed synchronously using an automatic
166 weather instrument (WXT530, Vaisala, Finland). All online data presented in this paper
167 were hourly averaged at local time (Beijing time, UTC+8).



168

169 **Figure 1.** Location of (a) the Yangtze River Delta (YRD) in China and (b) the sampling
170 site in Yangzhou (Maps were generated by using Arcgis Pro).

171 2.2 Data analysis

172 2.2.1 Satellite Product

173 Remote sensing of nitrogen dioxide (NO₂) and sulfur dioxide (SO₂) using satellite has
174 become a crucial tool for studying air pollution on a large spatial scale. In this study,
175 we utilized the Level 3 Near Real-Time Product of NO₂ (NRTI/L3 NO₂) obtained from
176 the TROPOspheric Monitoring Instrument (TROPOMI) with a spatial resolution of
177 3.5×7 km² to analyze the distribution of total vertical column of NO₂ (Cooper et al.,
178 2022). To avoid the obvious noises present in the NRTI/L3 SO₂ data over clean regions,
179 we employed the SO₂SMAS band from the Modern-Era Retrospective Analysis for
180 Research and Applications, version 2 (MERRA-2 SO₂SMAS) with a spatial
181 resolution of 69×55 km² to represent the distribution of SO₂ surface mass concentration
182 (Ukhov et al., 2020). We calculated and plotted the averaged 2-dimensional data of
183 NRTI/L3 NO₂ and SO₂SMAS during BLD and LD over the region of interest
184 (17.93~54.74 °N, 71.21~142.23 °E) using Google Earth Engine (Gorelick et al., 2017).
185 The integration of MERRA-2 and TROPOMI measurements has provided a more
186 comprehensive understanding of the sources and distributions of NO₂ and SO₂



187 facilitating the evaluation of the impact of human activities on air quality.

188 2.2.2 Geographic Source Analysis

189 The potential source contribution function (PSCF) analysis, based on the Hybrid
190 Single-Particle Lagrangian Integrated Trajectory (HYSPLIT) model, can be employed
191 to identify regional sources of air pollutants. Before conducting the PSCF analysis, 36
192 hours of air mass backward trajectories with one-hour resolution at 500 m above ground
193 level were calculated using the wind data from the Global Data Assimilation System
194 (GDAS) provided by the National Oceanic and Atmospheric Administration (NOAA)
195 (Wang et al., 2009). An open-source software Meteoinfo (Wang et al., 2014) was
196 utilized for the PSCF analysis. The whole study area (110.1~133.4 °E and 21.3~39.9
197 °N) covered by the trajectories was divided into thousands of cells with a spatial
198 resolution of $0.1^\circ \times 0.1^\circ$. The PSCF was simulated according to the following equation:

$$199 \quad PSCF_{ij} = \frac{m_{ij}}{n_{ij}} \quad (1)$$

200 where $PSCF_{ij}$ is the conditional probability that the grid cell (i, j) was a source of the
201 species found in high concentration (Hopke et al., 1993); n_{ij} is the number of all
202 trajectories passing through this grid cell, and m_{ij} is the number of trajectories. In this
203 study, the pollution criterion values for different BCc particle types were set as the 75th
204 percentile of hourly average number fractions, respectively. To further improve the
205 accuracy of the PSCF analysis and minimize analytical uncertainties, the Weighted
206 PSCF (WPSCF) functions as shown in Equation (2~3) were applied (Polissar et al.,
207 1999). The weight (W_{ij}) for each grid cell was determined based on the number of
208 trajectory endpoints (n_{ij}) as follows:

$$209 \quad WPSCF_{ij} = W_{ij} \times PSCF_{ij} \quad (2)$$

$$210 \quad W_{ij} = \begin{cases} 1.00 & n_{ij} > 3n_{ave} \\ 0.70 & 1.5n_{ave} < n_{ij} \leq 3n_{ave} \\ 0.40 & n_{ave} < n_{ij} \leq 1.5n_{ave} \\ 0.17 & n_{ij} \leq n_{ave} \end{cases} \quad (3)$$

211 Here, n_{ave} is the average number of trajectory endpoints of each grid.

212 2.2.3 SPA-MS Data Analysis

213 In total, 1649574 particles were analyzed during the entire observation period. The size
214 and chemical composition of single particles were analyzed using the Computational
215 Continuation Core (COCO V1.4) toolkit in MATLAB 2022 (The MathWorks, Inc.).
216 Our focus was on BCc particles, which were identified based on the relative peak area
217 (RPA) of carbon ion clusters (C_n^+ , $n = 1, 2, 3, \dots$), with a threshold of 0.05 (Zhang et al.,
218 2021). An adaptive resonance theory-based neural network algorithm (ART-2a) was
219 applied to classify the measured individual particles based on the presence and intensity
220 of ion peaks, with a vigilance factor of 0.75, a learning rate of 0.05, and 20 iterations
221 (Song et al., 1999).

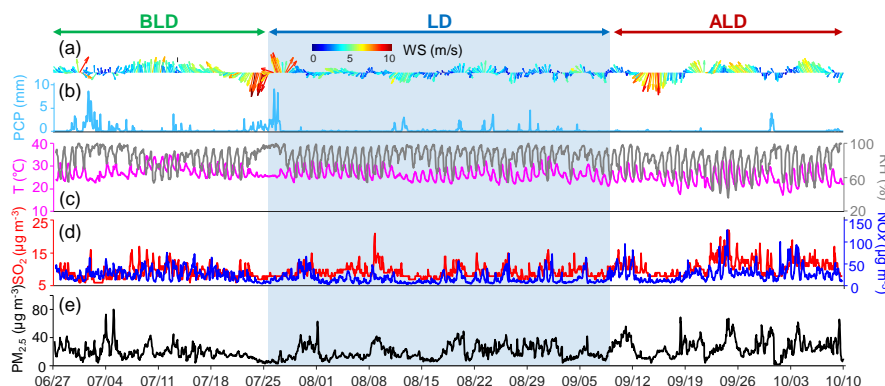


222 3. Results and discussion

223 3.1 Overview of field observations

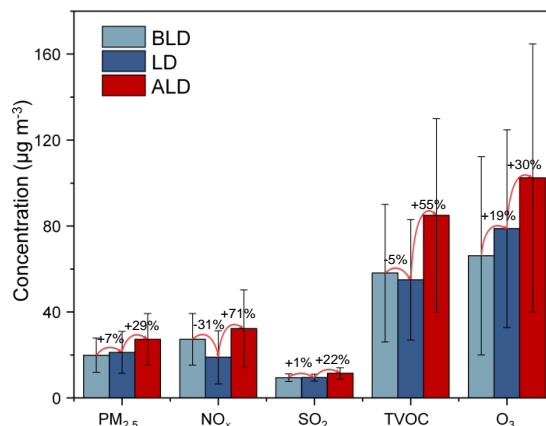
224 Figure 2 presents the temporal variations of meteorological parameters, PM_{2.5}, NO_x,
225 and SO₂ concentrations during the entire observation. During the BLD stage, the mean
226 temperature (T) was 28.2±2.6 °C, with an average relative humidity (RH) of 81.4±
227 11.1%. The prevailing winds originated from the south and southeast, with a mean wind
228 speed (WS) of 3.4±0.9 m s⁻¹. Notably, PM_{2.5}, NO_x, and SO₂ were dramatically reduced
229 at the end of the BLD period due to a high precipitation event, and the data collected
230 during the precipitation were excluded from the analysis. In comparison, the LD period
231 saw a decline in temperature to 26.2±2.4 °C, a reduction in WS to 2.3±0.8 m s⁻¹, and
232 an increase in RH to 86.6±10.1%. Additionally, Figures S2b~c exhibit uniform
233 distributions of RH and boundary-layer height (BLH) across the YRD during the LD
234 period. The resemblance of meteorological elements with other cities in the YRD (Qian
235 et al., 2022; Wang et al., 2022) and the effective removal of the pollutants accumulated
236 during the BLD stage imply that Yangzhou is mainly affected by upwind transmission
237 during the LD period, providing favorable conditions for investigating the regional
238 transport of BCc particles in the YRD during summer. Subsequently, the temperature
239 declined to 25.2±3.5 °C, the WS increased to 3.2±1.4 m s⁻¹, and RH decreased to a
240 lower level of 74.7±15.0% during the ALD period.

241
242 Further, surface concentrations of NO_x (18.9 µg m⁻³) and TVOC (55.0 µg m⁻³) were the
243 lowest during the LD period compared to those of the BLD and ALD periods, whereas
244 the surface O₃ concentration showed an increase of 12.6 µg m⁻³ (19%) during the LD
245 period compare to the BLD period, which may attribute to the reduction of fresh NO
246 emissions that alleviates O₃ titration (Steinfeld, 1998). However, the average
247 concentrations of PM_{2.5} (19.9 vs. 21.2 µg m⁻³) and SO₂ (9.4 vs. 9.5 µg m⁻³) were very
248 close between BLD and LD stages (Figure 3). Following the end of lockdown, social
249 activities gradually resume in Yangzhou City, leading to an apparent increase in all
250 observed pollutants during the ALD period. For instance, the relative increases from
251 LD to ALD were 71% for NO_x, 22% for SO₂, 55% for TVOC, 30% for O₃, and 29% for
252 PM_{2.5} (Figure 3), respectively.



253

254 **Figure 2.** Temporal variations of (a) wind direction (WD) and wind speed (WS), (b)
 255 precipitation (PCP), (c) temperature (T) and relative humidity (RH), (d) concentrations
 256 of NO_x and SO_2 , and (e) mass loading of $\text{PM}_{2.5}$.



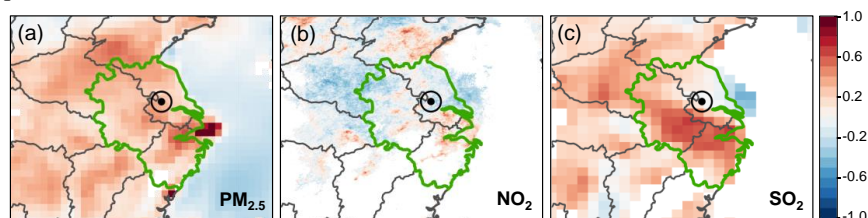
257

258 **Figure 3.** Ground-based observations of $\text{PM}_{2.5}$, NO_x , SO_2 , O_3 , and TVOC
 259 concentrations in Yangzhou. The figure compares the averages during the BLD (blue-
 260 grey), LD (dark-blue), and ALD (crimson) periods. Error bars indicate SDs over
 261 different lockdown periods.

262 In addition to ground measurements, satellite retrieved $\text{PM}_{2.5}$, NO_2 , and SO_2 data over
 263 the entire region of eastern China were also investigated. Results show that the hotspots
 264 of those pollutants were predominantly located over eastern China, e.g., the YRD region,
 265 during both the BLD and LD periods (Figure 3). Figure 4 displays the regional
 266 fractional changes in mean $\text{PM}_{2.5}$, NO_2 , and SO_2 levels from the BLD to LD periods in
 267 the YRD, indicating a 29%, 25%, and 23% increase, respectively. In comparison,
 268 Yangzhou city experienced lower increases in these air pollutants, with changes of 25%,
 269 -23.8%, and 2.9% for $\text{PM}_{2.5}$, NO_2 , and SO_2 , respectively (remarkable NO_2 decrease).
 270 Such results highlight the short-term, limited-scale, and human-induced reduction in air
 271 pollutants as a result of the lockdown measures in Yangzhou, and demonstrate the



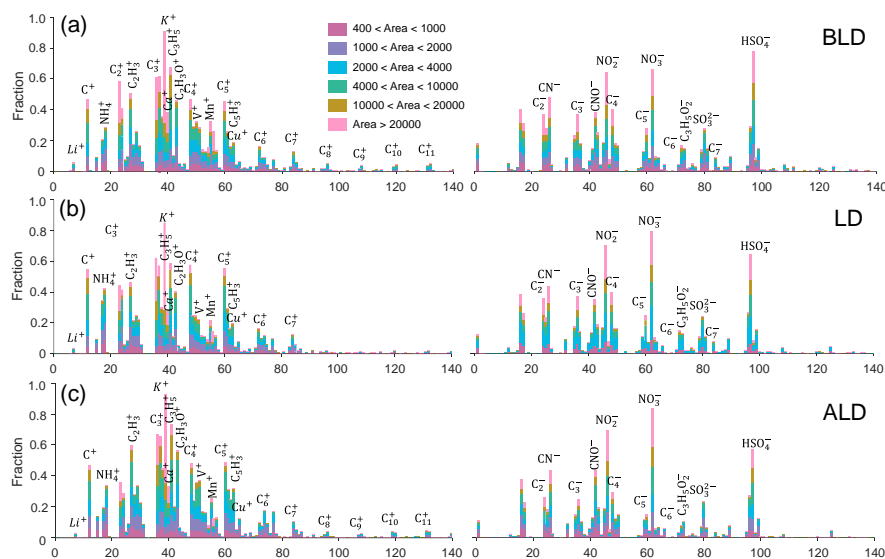
272 effectiveness of regional stringent emission control in reducing local atmospheric
273 pollutant concentrations.



274
275 **Figure 4.** The fractional changes (i.e., $100 \times (\text{LD} - \text{BLD}) / \text{BLD}$) of (a) $\text{PM}_{2.5}$, (b) NO_2 ,
276 and (c) SO_2 between BLD and LD periods based on spaceborne measurement.
277 Calculations were only conducted for the regions with $\text{PM}_{2.5} > 10 \mu\text{g m}^{-3}$, $\text{NO}_2 > 0.2$
278 Dobson units (DU), and $\text{SO}_2 > 0.2$ DU in the BLD period. The circle symbols in the
279 maps indicate the location of Yangzhou, and the green region represents the YRD (1
280 $\text{DU} = 0.4462 \text{ mmol m}^{-2}$).

281 3.2 Chemical composition and size distribution of individual 282 BCc particles

283 Based on the SPA-MS analysis, a total of 1068362 BCc particles were collected over
284 the whole study period. The BCc particles accounted for 58.8%, 67.7%, and 56.5% of
285 the total number of measured particles in the BLD, LD, and ALD periods, respectively.
286 Figure 5 shows the normalized average mass spectra of BCc particles during three
287 periods. Ion height in each spectrum reflects the number fraction of the detected BCc
288 particles with the corresponding ion to the total BCc particles, while colors represent
289 peak area ranges of detected ions. As shown in Figure 5, BCc particles in BLD, LD,
290 and ALD shown similar mass spectra at $m/z < 100$, with common peaks including
291 carbon ion clusters (C_n^+ , $n = 1\sim 7$), $27[\text{C}_2\text{H}_3]^+$, $37[\text{C}_3\text{H}]^+$, $43[\text{C}_2\text{H}_3\text{O}]^+$, $51[\text{C}_4\text{H}_3]^+$,
292 $63[\text{C}_5\text{H}_3]^+$, $46[\text{NO}_2]^-$, $62[\text{NO}_3]^-$, and $97[\text{HSO}_4]^-$. However, the abundance of large m/z
293 carbon ions (C_n^+ , $n > 7$) in both BLD and ALD periods was approximately 1.5 times that
294 in the LD. The result was a clear reflection of less local vehicle emissions during the
295 LD period (Liu et al., 2019), in line with aromatics, e.g., $119[\text{C}_9\text{H}_{11}]^+$.



296

297 **Figure 5.** The average positive and negative mass spectra of BCc particles **(a)** before
 298 the lockdown period (BLD), **(b)** during the lockdown period (LD), and **(c)** after the
 299 the lockdown period (ALD).

300

301 BCc particles were further classified into 12 types based on the differences of chemical
 302 features and temporal variations as shown in Table S1. Fresh BC particles (BC-fresh)
 303 are those freshly emitted without undergoing significant atmospheric processing (Ding
 304 et al., 2021). Five types of BC-fresh particles were identified according to the
 305 characteristics ion markers: (i) BC-pure is dominated by carbon clusters (C_n^\pm) with
 306 minor ion signals of secondary inorganic species, such as $46[NO_2]^-$ and $97[HSO_4]^-$
 307 from nitrate and sulfate, respectively (Xie et al., 2020); (ii) BCc particles from biomass
 308 burning (BB) are characterized by ion signals at m/z $39[K]^+$, $45[CHO_2]^-$, $59[C_2H_3O_2]^-$,
 309 and $73[C_3H_5O_2]^-$, with relative peak area (RPA) more than 0.5 (Silva et al., 1999); (iii)
 310 coal combustion BCc particles (CC) typically include small carbon clusters (C_n^\pm , $n =$
 311 $1\sim 4$), metal elements (e.g., $7[Li]^+$, $23[Na]^+$, $27[Al]^+$, $56[Fe]^+$, $63[Cu]^+$ and
 312 $206/207/208[Pb]^+$), and organic carbon ($38[C_3H_2]^+$, $43[C_2H_3O]^+$) peaks in the positive
 313 mass spectrum, while the strong signals of secondary inorganic species ($46[NO_2]^-$,
 314 $43[AlO]^-$, $62[NO_3]^-$, $80[SO_3]^-$, $97[HSO_4]^-$) in the negative ion mode suggest that CC
 315 particles were long-distance transported or more processed (Zhang et al., 2022; Zhang
 316 et al., 2009); (iv) particles from vehicle emission (VE) are characterized by the presence
 317 of ion signals at m/z of $40[Ca]^+$, $51[V]^+$, $55[Mn]^+$, $67[VO]^+$, $46[NO_2]^-$, $62[NO_3]^-$, and
 318 $79[PO_3]^-$, as well as high loadings of organic carbon ($41[C_3H_5]^+$, $43[C_2H_3O]^+$) and
 319 carbon clusters (C_n^\pm , $n = 1\sim 4$) ion peaks (Yang et al., 2017); (v) BCc particles that are
 320 internally mixed with more than one type (BB, CC, and VE) are categorized as Mix
 321 type (Sun et al., 2022).

322



323 Aged BC particles, denote as BC-aged, undergo a series of chemical reactions and
324 physical transformations. These processes typically lead to changes in their morphology,
325 hygroscopicity, and optical properties as they are coated with other materials (He et al.,
326 2015). Six types of BCc particles are classified as BC-aged and are further grouped into
327 BCOC and BC-SNA, depending on whether they contain mainly organic carbon (OC)
328 or sulfate/nitrate/ammonium (SNA). First, BCOC types indicate BC-aged particles that
329 internally mixed with OC. These particles are characterized by the presence of carbon
330 clusters (C_n^+) and $C_nH_m^+$ ions ($n = 1\sim6$, $m = 1\sim3$) in positive mass spectra (Xie et al.,
331 2020). On the other hand, BC-aged particles that do not mix with OC are named BC-
332 SNA indicating the mix with secondary inorganic species. Additionally, BCOC
333 particles with negative mass spectra dominated by nitrate ions ($46[NO_2]^-$ and $62[NO_3]^-$)
334 or sulfate ions ($97[HSO_4]^-$) are referred to as BCOC-N or BCOC-S, respectively;
335 otherwise, BCOC particles showing similar peak areas of nitrate and sulfate are named
336 BCOC-SN. Furthermore, The BC-SNA particles are further categorized as BC-N, BC-
337 S, and BC-SN based on similar principles. Note the remaining particles that cannot be
338 classified into neither BC-fresh or BC-aged ones are denoted as BC-other. More details
339 of BCc particle types are shown in Table S1 and Figure S1 in the Supplement.

340
341 During the BLD period, the average number fraction of BC-fresh particles was 36%
342 with sizes mainly concentrated at ~ 500 nm, while the mode size of BC-aged particles
343 was ~ 520 nm (Figure 7). The predominant BCc types during the BLD period were
344 BCOC-S and BC-S (24% and 12% by number), likely because sulfate was removed
345 less efficiently than organic matter (OM) and NO_3 by heavy precipitation, especially
346 during the warm seasons (Isokääntä et al., 2022). As shown in Figure 7c and d, the peak
347 size of BC-SNA was larger than that of BCOC in all periods, indicating that organics
348 coated BCc generally had a relatively thin coating compared to those coated by
349 secondary inorganic species, which is consistent with previous studies (Sun et al., 2016;
350 Wang et al., 2019).

351
352 During the transition of BLD period ($PM_{2.5}$: $19.9 \mu g m^{-3}$, O_3 : $66.2 \mu g m^{-3}$, NO_x : $27.3 \mu g$
353 m^{-3}) to LD period ($PM_{2.5}$: $21.2 \mu g m^{-3}$, O_3 : $78.8 \mu g m^{-3}$, NO_x : $18.9 \mu g m^{-3}$), heavy
354 precipitation occurred on July 28th (the day before lockdown) and scavenged a majority
355 of the pollutants ($PM_{2.5}$: $4 \mu g m^{-3}$, O_3 : $35 \mu g m^{-3}$, NO_x : $8 \mu g m^{-3}$). After that, the strict
356 lockdown measures were carried on and the primary emissions were abruptly cut down.
357 As a result, the number fraction of BC-fresh particles significantly decreased from 37%
358 to 28% and that of VE-type particles dropped from 12% to 3% (by number). As shown
359 in Figure 3, with the decrease in NO_x , an obvious enhancement of O_3 was observed
360 during the LD period. According to previous studies (Huang et al., 2021; Laughner et
361 al., 2021), large reduction of NO_x could promote the formation of O_3 under a VOC-
362 limited regime and enhance the oxidation capacity of the local atmosphere, which made
363 the number fraction of BC-aged particles increased from 64% in the BLD to 72% in the
364 LD period (Figure 6a), indicating the lockdown measures could accelerate aging of BCc



365 particles through complicated chemical reactions and/or physical coagulation. We also
366 found the most abundant type of BCc particles changed from BCOC-S (24% by number)
367 in the BLD to BC-N (25%) in the LD (Figure 6a). Furthermore, despite the abrupt
368 reductions of NO_x due to city lockdown, it should be aware that the PM_{2.5} concentration
369 slightly increased during the LD period, highlighting the non-linear relationship
370 between primary emissions and PM_{2.5} levels.

371

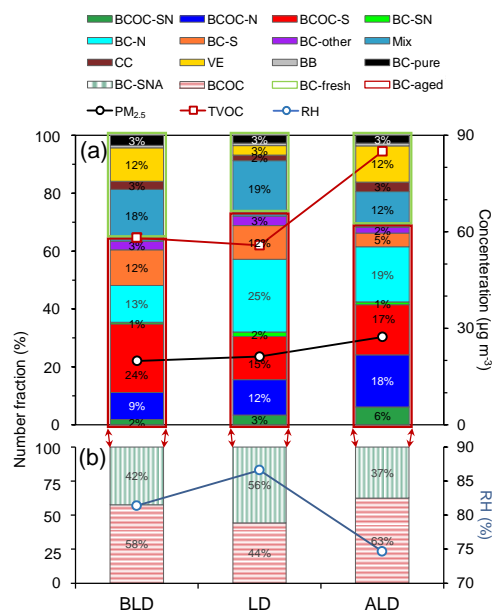
372 During the ALD period (PM_{2.5}: 25.9 μg m⁻³, NO_x: 27.9 μg m⁻³, TVOC: 76.4 μg m⁻³),
373 the number fraction of BC-fresh particles increased from 28% to 31%, and the fraction
374 of VE particles also increased from 3% to 12% (by number) (Figure 6a). Notably, the
375 size distributions of BC-fresh and BC-aged particles presented relatively small peaks
376 at 690 nm and 820 nm during the ALD period, in addition to the prominent peaks at
377 490 nm and 500 nm, which were different from those in the BLD and LD periods. These
378 small peaks were relatively close to the dominant sizes of BC-fresh and BC-aged
379 particles during the LD period (Figure 7). This result suggests that a substantial number
380 of BCc particles with small sizes (around 500 nm) after the lockdown was lifted in
381 Yangzhou, owing to the sudden enhancement of primary emissions; on the other hand,
382 particles with large diameters (>690 nm) may have formed due to the participation of
383 more trace reactive gases (e.g., NO_x, SO₂, and VOCs) in continuous aging reactions,
384 resulting in thicker coatings on the surface of pre-existing particles and therefore a more
385 clear separation of two mode sizes during the ALD period than during the other two
386 periods. This hypothesis was also supported by the increased number fraction of
387 BCOC-SN during the ALD period (Figure 6a). Similar findings have been reported in
388 the North China Plain (NCP) and the YRD during cold seasons, where thicker coatings
389 on secondary aerosols were also observed under lower RH (<70%) (Zhang et al., 2021).
390 This might be due to that particles with more organics and nitrate can result in earlier
391 deliquescence and provide aqueous surfaces that facilitates heterogeneous formation of
392 secondary species under relatively low RH (Zhang et al., 2021). Among the three
393 periods, the difference between the mode sizes of BC-aged and BC-fresh particles was
394 the smallest (10 nm) during the ALD period (Figure 7a and b). This size reduction can
395 be attributed to the increased BCOC and hydrophobic primary particles after lockdown
396 (Figure 6). Because the internally mixed BCOC and hydrophobic primary particles may
397 constrain further growth of secondary BC-SNA particles (Liu et al., 2016; Zhang et al.,
398 2018), thereby leading to smaller-sized BC-aged particles. Moreover, the differences of
399 BCc mode sizes between ALD and BLD periods also reveals an interesting fact that the
400 lockdown effect may not only affect air quality during lockdown, but also can influence
401 the air quality even after lockdown, as the resumed emissions after lockdown may be
402 subjected to different chemistry from that before lockdown.

403

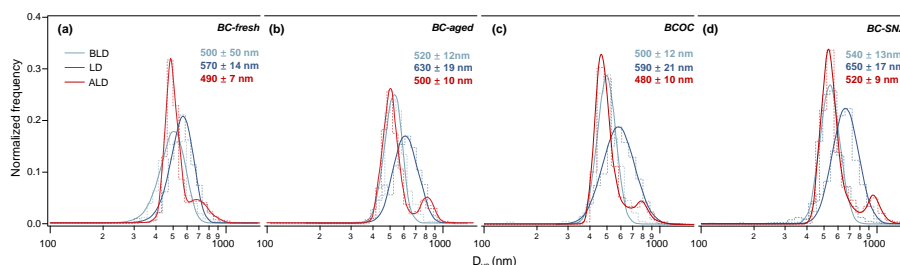
404 Throughout the entire observation, the changes in the number fraction of BC-SNA
405 showed consistency with the variations in RH (Figure 6b), indicating that BC tends to
406 mix with ammonium sulfate and ammonium nitrate under high RH conditions overall.



407 Meanwhile, the number fraction of BCOC had similar patterns of change as TVOC,
 408 suggesting that high TVOC levels may facilitate the coating of organics on BC cores.
 409 Figure 8 displays the number fraction of BCc species as a function of PM_{2.5}. Overall,
 410 as PM_{2.5} levels increased, the number fraction of BC-aged particles also increased,
 411 while the proportion of BC-fresh particles decreased during the BLD and LD periods,
 412 indicating a clear transition from BC-fresh particles to more aged ones. However, the
 413 increase in PM_{2.5} was driven by BCOC-S during the BLD period (Figure 8a), whereas
 414 BC-N played a vital role in the PM_{2.5} increase during the LD period (Figure 8b).
 415 Interestingly, the concentration of NO_x, the primary precursor of BC-N, decreased by
 416 31% and 41% during the LD period compared to the BLD and ALD periods,
 417 respectively (Figure 3). Despite the significant decrease, the proportion of BC-N during
 418 the LD period was unexpectedly higher than those during the BLD and ALD periods,
 419 indicating a strong non-linear response of nitrate in BCc particles to NO_x, very likely
 420 due to much faster conversion of NO_x to nitrate upon enhanced atmospheric oxidation
 421 capacity; additionally, the high proportion of BC-N during the LD period might be
 422 attributed to regional transport, similar to that in Shanghai during 2020 winter lockdown
 423 (Chang et al., 2020).



424
 425 **Figure 6.** Number fractions of BCc particles. (a) The number fractions of different BCc
 426 particles along with the concentrations of PM_{2.5} and total volatile organic compounds
 427 (TVOC). (b) The number fractions of different types of BC-aged particles along with
 428 relative humidity (RH).



429

430

431

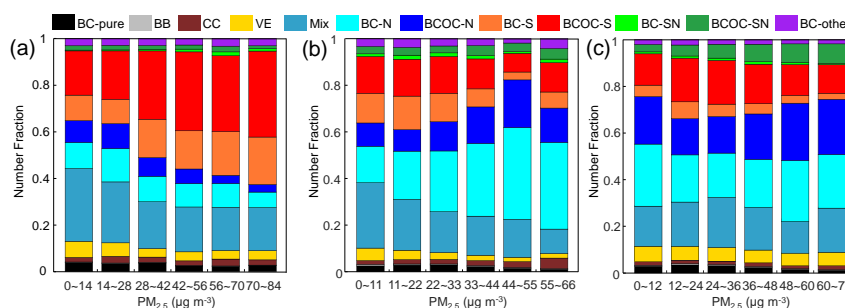
432

433

434

435

Figure 7. Size distribution of different types of BCc particles during different lockdown in Yangzhou. **(a)** BC-fresh particles, **(b)** BC-aged particles, **(c)** BCOC particles, and **(d)** BC-SNA particles. The Log-normal distribution was used to fit the unimodal size distribution, and the Lorentz distribution was used to fit the bimodal size distribution. The corresponding mode sizes (with the standard deviations) are also shown.



436

437

438

Figure 8. Variations of number fractions of BCc particle types with $PM_{2.5}$ mass concentrations during **(a)** the BLD period, **(b)** the LD period, and **(c)** the ALD period.

439

3.3 Chemical aging of BCc Particles

440

441

442

443

444

445

446

447

448

449

450

451

452

453

454

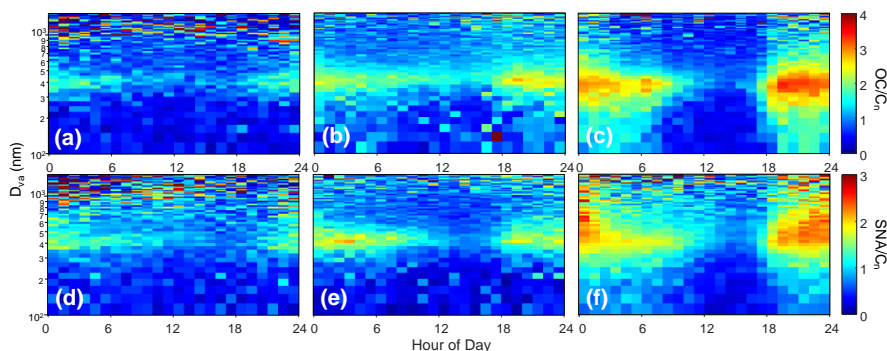
455

As shown in Figure 5, in the average positive mass spectra of total BCc particles, the peak areas of C_n^+ , OM, and metals contributed to more than 95% of the total, while nitrate and sulfate peak areas accounted for more than 90% of the negative mass spectral signal. To better elucidate the aging processes of BCc particles during different lockdown periods, we summed the carbon clusters C_n^+ ($n = 1\sim 5$, accounting for more than 99% of C_n) peak areas to represent BC, and the total peak area of sulfate, nitrate, and ammonium (SNA) to represent the second inorganic components coated on BC. Additionally, we defined the sum of positive peak areas, excluding C_n^+ and metals, as OC to represent the OM coated on BC. These peak areas encompassed almost all the coating materials, except for metals, of BCc particles. The changes in the mixing state and morphology of BCc particles can provide insights into their aging characteristics, as reported previously (Kandler et al., 2018; Moffet et al., 2013). In this study, we use OC/C_n and SNA/C_n ratios to describe different types of chemical components coated on BC-fresh, and we use the ratio of the mode size of BC-aged (D_{aged}) to that of contemporaneous BC-fresh (D_{fresh}) to represent the aging degree of BCc particles.



456 Figure 9 illustrates the diurnal variations of the OC/C_n and SNA/C_n ratios along with
457 the size distribution of BCc particles during different periods. Throughout the entire
458 observation, we observed that both OC/C_n and SNA/C_n increased during nighttime and
459 decreased during daytime. These variations showed the prominent enhancements of
460 nocturnal OM and SNA, which could be attributed to the accelerated gas-to-particle
461 partitioning and nocturnal secondary formation of organic/inorganic components under
462 high relative humidity ($RH > 85\%$) and relatively stagnant air ($WS < 3 \text{ m s}^{-1}$) (Figure
463 S4). It is worth noting that from the BLD period to the LD and ALD periods, the
464 intensity of diurnal variations of OC/C_n and SNA/C_n increased obviously. This
465 discrepancy can attribute to several reasons. During the BLD period, the frequent
466 precipitations effectively scavenged the particles (Isokääntä et al., 2022). In contrast,
467 stronger solar radiation and higher ozone level during the LD period promoted
468 photochemical formations of OC and SNA; After lockdown, more precursors due to
469 increased local emissions may lead to more production of secondary components than
470 that during the BLD period as explained earlier. These results indicate that the aging
471 process and mixing state of BCc particles depend strongly on weather conditions and
472 anthropogenic emission structures in urban cities.

473
474 As shown in Figure 9, BCc particles with $\sim 400 \text{ nm } D_{va}$ exhibited significant diurnal
475 fluctuations in the OC/C_n and SNA/C_n ratios, during the LD period. Moreover, there
476 was a noticeable increase in the proportion of BC-SNA particles during nighttime when
477 RH was relatively high. These observations suggest that nighttime heterogeneous
478 hydrolysis may be considered as a key mechanism responsible for the formation of
479 BCOC and BC-SNA particles. According to Jacobson (2002), coagulation can be
480 significant between particles with sizes $< 100 \text{ nm}$ and $> 1 \mu\text{m}$ but insignificant for
481 particles of $> 300 \text{ nm}$, when the total particle number concentration is higher than
482 10^4 cm^{-3} . During the LD period, the OC/C_n and SNA/C_n ratios of BCc particles with
483 $\sim 400 \text{ nm } D_{va}$ exhibited pronounced diurnal variations (Figure 9) and the number
484 fraction of BC-SNA increased obviously. Despite the difference between D_{va} and
485 physical diameter, such results imply that chemical reactions should be considered as
486 the major pathway for BCOC and BC-SNA particles of $\sim 400 \text{ nm } D_{va}$, while the large-
487 sized BC-aged particles ($> 1 \mu\text{m}$) may be partially from physical coagulation. Moreover,
488 the larger peak D_{va} ($\sim 600 \text{ nm}$) and higher D_{aged}/D_{fresh} ratios (1.11) were observed
489 compared to those of the BLD ($\sim 510 \text{ nm}$, 1.03) and the ALD periods ($\sim 500 \text{ nm}$, 1.02)
490 (Figure 7). Since RH was significantly higher during LD period (average RH of 86.6%)
491 than the BLD period (average RH of 81.4%) and ALD period (average RH of 74.7%),
492 this result again supports that aqueous or heterogeneous reactions might play a more
493 important role to facilitate the chemical conversion of trace reactive gases (e.g., SO_2 ,
494 NO_x , and VOCs) and then formed a thicker coating on the surfaces of BC cores, leading
495 to evident growth in the size of BCc particles. In addition, this aqueous or
496 heterogeneous process during the LD period likely converted partially coated particles
497 to fully thickly coated BCc particles as well (Figure 11).



498

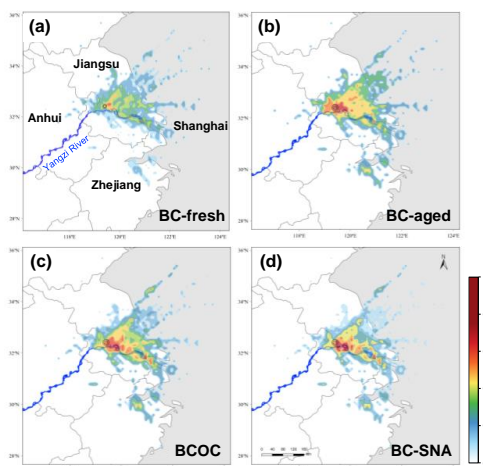
499 **Figure 9.** Diurnal variations of the ratios of OC/C_n and SNA/C_n with a size distribution
500 of BCc particles during (a, d) the BLD period, (b, e) the LD period, and (c, f) the ALD
501 period.

502 3.4 Source of BCc particles during lockdown

503 In addition to local emissions, regional transport plays a significant role in influencing
504 the pollutant levels. Due to the emergent lockdown in Yangzhou, local emissions were
505 strictly limited, while surrounding cities were still as usual, it is therefore interesting to
506 investigate source areas of BCc sources under such scenario. Besides, the air pollutants
507 were significantly influenced by regional transport, presenting an ideal opportunity to
508 investigate the transmission and source characteristics of BCc particles in the YRD
509 during summer. Here, the PSCF method was used to qualitatively simulate the source
510 probability distributions of the specific BCc particle types (BC-fresh, BC-aged, BCOC,
511 and BC-SNA) during the LD period. The results of the potential source regions and
512 clustering analysis are presented in Figure 10.

513

514 As shown in Figure 10, the hotspots of potential sources for the four particle types
515 exhibited strong agreements with each other and primarily concentrated in the southeast
516 of Yangzhou, especially along the coast of the Yangtze River, with the WPSCF greater
517 than 0.6. These hotspot areas also encompassed chemical enterprises, power plants,
518 petrochemical industrial parks, and the Yangtze River Ship Channel in the YRD.
519 Moreover, BCc particles and gaseous emissions from the YRD city cluster, heavy
520 industries, and ship diesel engines, can easily impact the air quality of surrounding
521 downwind regions. This evidence suggests that the region of southeast Yangzhou and
522 lower reaches of Yangtze River are major source areas for the regionally transported
523 BCc particles in Yangzhou during lockdown.



524

525

526

Figure 10. The potential sources areas of different BCc particles during the LD period. **(a)** BC-fresh. **(b)** BC-aged. **(c)** BCOC. **(d)** BC-SNA.

527

528

529

530

531

532

533

534

535

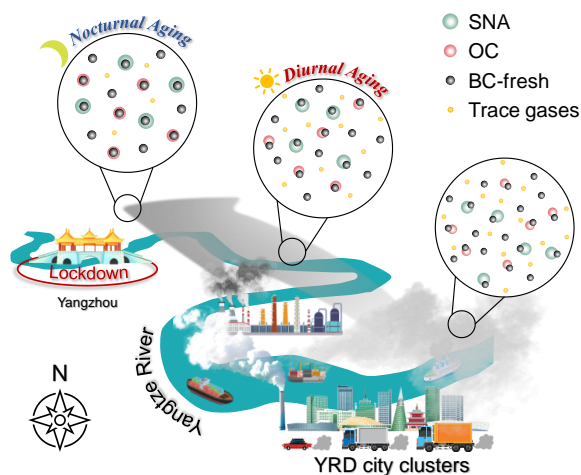
536

537

538

539

According to Luo et al. (2023), regional transport of pollutants can occur near surface from upwind areas when the wind speed (WS) exceeds 2 m s^{-1} . Figure S4b shows that the mean daytime WS was 3 m s^{-1} , indicating that both BC-fresh and BC-aged particles, along with trace gases (e.g., SO_2 , NO_x , and VOCs), originating from the hotspot areas, could be transported effectively to Yangzhou. Additionally, the average size of BCc particles remained around $0.6 \mu\text{m}$ at daytime (Figure S4c), suggesting that BCc particles could undergo continual aging reactions under relative lower RH, but producing relatively thinly coated BCc particles with smaller sizes than those at nighttime (average size of $0.65 \mu\text{m}$) (Figure 11). The mean nocturnal WS decreased to 2 m s^{-1} , indicating that the regional atmosphere becomes stagnant (Figures S4a, b). As mentioned earlier and underscored here again, this stagnant and humid atmospheric condition may promote aqueous or heterogeneous reactions, likely further leading to the production of more thickly coated BCc particles than daytime ones (Figure 11).



540
541 **Figure 11.** A schematic diagram of the transportation of air pollutants and ageing
542 process from the YRD city cluster to Yangzhou during the 2021 summer COVID-19
543 lockdown.

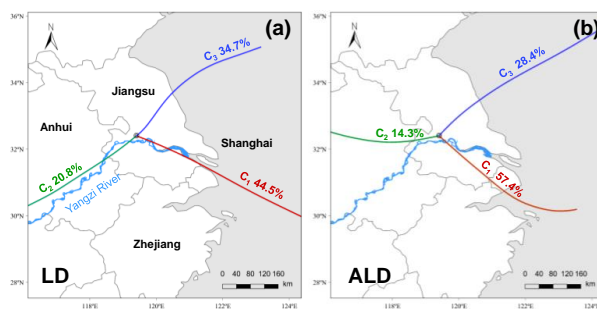
544 3.5 Local and non-local source analysis

545 Since there was a heavy precipitation on July 28th (the day before lockdown) which
546 removed most atmospheric pollutants, the air pollutants might be influenced mostly by
547 regional transport as local emissions were significantly cut down during the LD period.
548 As a comparison, the pollution during the ALD period might be caused by both local
549 emissions and regional transport. Additionally, the meteorological conditions were
550 relatively stable during the LD and ALD periods (Figure 2a~c); the trajectories of these
551 two periods were both categorized into similar 3 clusters, indicating stable regional
552 transport of the pollutants from the southeast, southwest, and northeast (Figure 12). The
553 lockdown event with favorable meteorological conditions provided a valuable
554 opportunity to investigate emissions-meteorology interactions in YRD during summer.
555 Here, we propose a method to roughly estimate the local and non-local proportions of
556 for each type of BCc particles in Yangzhou during the ALD period (representing the
557 usual emission condition)

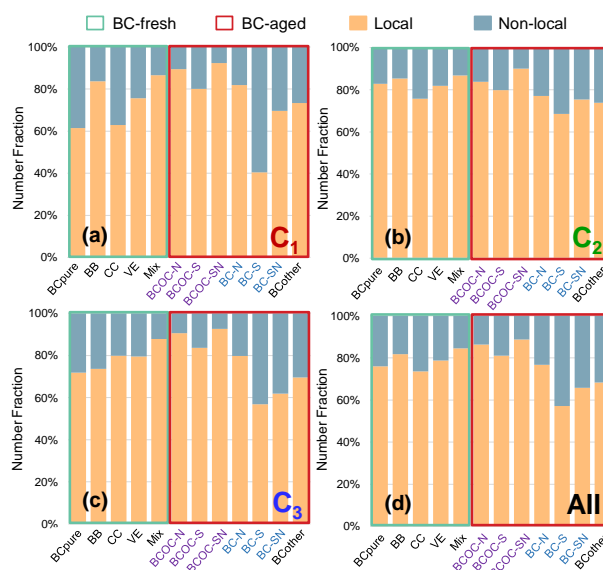
$$558 \quad [PM]_{i,j}^{non-local} = [PM]_{i,j}^{LD} \times t_i^{ALD} / t_i^{LD}; \quad (4)$$

$$559 \quad [PM]_{i,j}^{local} = [PM]_{i,j}^{ALD} - [PM]_{i,j}^{non-local}. \quad (5)$$

560 For Equation (4~5), the duration of the i^{th} cluster in different periods is represented by
561 t_i^{LD} and t_i^{ALD} . The sum of the hourly number density of the j^{th} type of particulate matter
562 in the i^{th} cluster during the LD period is denoted as $[PM]_{i,j}^{LD}$. Similarly, $[PM]_{i,j}^{non-local}$
563 and $[PM]_{i,j}^{local}$ indicate the summed hourly number density of specific types of BCc
564 particles from non-local and local sources in the i^{th} cluster during the ALD period,
565 respectively.



566
 567 **Figure 12.** Back-trajectory analysis during (a) LD and (b) ALD period. The
 568 corresponding percentages of total trajectories for Cluster1 (C₁, red), Cluster2 (C₂,
 569 green) and Cluster3 (C₃, blue) are also shown.



570
 571 **Figure 13.** Number fraction of local and non-local in different types of particles in (a)
 572 Cluster1 (C₁), (b) Cluster2 (C₂), (c) Cluster3 (C₃), and (d) all clusters during the ALD
 573 period. The purple labels represent BCOC particles and the blue labels represent BC-
 574 SNA particles.

575
 576 By using this method, analysis results of the sources of all types of BCc particles from
 577 different clusters are presented in Figure 13a~c. Cluster1 (C₁), originating from the
 578 economically developed southeast region, accounted for 57.4% of total trajectories
 579 during the ALD period. C₁ exhibited the highest proportions of non-local fresh BCc
 580 (BC-pure, 38.6%) and coal combustion BCc (CC 37.1%), along with vehicular ones
 581 (VE 24.3%), underscoring the substantial impact of heavy industry and transportation
 582 from the southeastern YRD during summer (Figure 13b). Notably, non-local
 583 contribution of BC-S was dominant in C₁, indicating significant regionally transported
 584 sulfate. Cluster2 (C₂), originating from the southwest region covering Nanjing and



585 eastern Anhui province, accounted for 14.3% of all trajectories (Figure 12b). The non-
586 local proportions for all particle types were around 20%, indicating that local emission
587 was dominant (Figure 13b). Cluster 3 (C_3), originating from the East China Sea and
588 passing through the vast cultivated area in northeastern Jiangsu Province, contributed
589 28.4% of the total trajectories (Figure 12b). A relatively high proportion of BCc
590 particles generated by non-local biomass-burning emissions (BB, 26.4%) was observed
591 in C_3 , indicating a correlation between BCc particles from the northeastern YRD and
592 open-field burning of agricultural residues during summer (Figure 13c).

593
594 Regarding the number fraction of local and non-local contributions for the whole
595 campaign (Figure 13d), the proportion of local BC-N particles (~80%) exceeded that
596 of BC-S (~60%; note non-local contribution of BC-S even dominated over local
597 counterpart in C_1), suggesting that sulfate-associated BCc particles were more likely
598 from regional transport than those of nitrate-associated ones. The proportion of non-
599 local BC-aged particles was relatively higher than the BC-fresh particles naturally, as
600 BC-aged particles intercepted more secondary species during the regional transport
601 than freshly emitted BCc particles. Furthermore, the proportion of local BCOC particles
602 exceeded that of BC-SNA particles, implying a strong relationship between BCOC
603 particles and local emission, whereas more BC-SNA particles were likely associated
604 with regional transport. Overall, BCc particles was predominantly local (78%) in
605 Yangzhou during normal summertime. However, BCc particle from coal combustion
606 (CC, 26%) and vehicle emission (VE, 21%) transported from the southeast, as well as
607 biomass burning-related emissions (BB, 19%) from the northeast, were also significant
608 contributors that should not be ignored (Figure 13d). These findings highlight the
609 importance of considering both local and regional sources, as well as understanding the
610 transport characteristics of different types of BCc particles for air quality management.

611 **4. Conclusions and implications**

612 During the summer of 2021, the COVID-19 lockdown imposed in Yangzhou resulted
613 in a significant decrease in anthropogenic emissions from traffic and manufacturing
614 sectors. To examine the effects of this lockdown, we utilized spaceborne observations,
615 ground-based measurements, and particularly SPA-MS analysis to explore the
616 variations, aging characteristics, and sources of BCc particles in the YRD. We showed
617 that the strict emission controls effectively reduced local gaseous pollutants. However,
618 the decline in NO_x (-30.1%) and TVOC (-5.3%) levels might on the other hand result
619 in increased ozone (+19.0%), leading to a rise in BC-aged particles and a slight
620 elevation in $\text{PM}_{2.5}$ levels during the lockdown. Our results revealed a strong non-linear
621 response of $\text{PM}_{2.5}$ and O_3 to the gaseous precursors.

622
623 The SPA-MS analysis results further demonstrate significant enhancement of OM and
624 SNA coating species on BC-fresh particles, owing to gas-to-particle partitioning and
625 nocturnal multiphase chemistry. Consequently, we observed a higher fraction of BC-



626 aged particles (73%) during the lockdown due to enhanced oxidizing capacity and high
627 relative humidity (RH > 85%). The BC-fresh particles tended to mix with SNA under
628 high RH conditions, while high TVOC levels were accompanied by BCOC formation.
629 However, BCOC particles generally exhibited smaller sizes compared to BC-SNA
630 particles. Moreover, we postulate that aqueous or heterogeneous reactions might be
631 important to generate BCOC and BC-SNA particles, especially ones with ~400 nm D_{va} ,
632 while coagulation might play a more prominent role in larger BC-aged particles. The
633 aging process during the LD period promoted the conversion of partly coated particles
634 to totally coated ones, with larger diameters (~600 nm) and thicker coatings.

635

636 Furthermore, our study highlights that local emissions were the main source of BCc
637 particles in Yangzhou during normal summertime. However, regional transported coal
638 combustion (23%) and vehicle emissions (21%) from southeast, as well as biomass
639 burning emissions (19%) from the northeast, were also significant. Meteorological
640 conditions, including wind patterns and relative humidity, also influenced the regional
641 transport of BCc particles in the YRD.

642

643 It should be noted that the observed average $PM_{2.5}$ concentration during the lockdown
644 in Yangzhou was $21.2 \mu\text{g m}^{-3}$, which still significantly exceeds the WHO's air quality
645 guideline of $5 \mu\text{g m}^{-3}$. Our research highlights that reduction of local primary emissions
646 from traffic and manufacturing sectors alone has limited effect in air quality
647 remediation. Complex chemistry, regional transport and meteorological factors need to
648 be considered cooperatively. Therefore, we suggest a more comprehensive regulation
649 of precursor gases from multiple sectors, a wide-ranging joint regulation approach as
650 well as proper consideration of the chemistry, so as to develop an effective strategy for
651 air quality improvement.

652

653 **Data availability.** Data described in this manuscript can be accessed at repository under:
654 <https://doi.org/10.6084/m9.figshare.24427795> (Dai, 2023)

655

656 **Author contributions.** XG and YD designed the research. YD, HW and SC conducted
657 the field measurements. YD, HW, JW and SC analyzed the data. XG, JW, HL, YW, YZ,
658 and EA reviewed the paper and provided useful suggestions. YD and XG wrote the first
659 draft of paper. All people involve in discussion of the results.

660

661 **Supplement.** The supplement related to this article is available online at: XXX.

662

663 **Competing interests.** The contact author has declared that neither they nor their co-
664 authors have any competing interests.

665

666 **Financial support.** This research has been supported by the National Natural Science
667 Foundation of China (grant nos. 42377100 and 42021004).



668 **References**

- 669 Bond, T.C., Doherty, S., Fahey, D.W., Forster, P., Berntsen, T., DeAngelo, B., Flanner,
670 M., Ghan, S., Kärcher, B., Koch, D., Kinne, S., Kondo, Y., Quinn, P.K., Sarofim,
671 M., Schultz, M., Michael, S., Venkataraman, C., Zhang, H., Zhang, S., Zender,
672 C.S., 2013. Bounding the role of black carbon in the climate system: A Scientific
673 assessment. *Journal of Geophysical Research: Atmospheres* 118, 5380–5552.
674 <https://doi.org/10.1002/jgrd.50171>
- 675 Cappa, C.D., Zhang, X., Russell, L.M., Collier, S., Lee, A.K.Y., Chen, C.-L., Betha, R.,
676 Chen, S., Liu, J., Price, D.J., Sanchez, K.J., McMeeking, G.R., Williams, L.R.,
677 Onasch, T.B., Worsnop, D.R., Abbatt, J., Zhang, Q., 2019. Light Absorption by
678 Ambient Black and Brown Carbon and its Dependence on Black Carbon
679 Coating State for Two California, USA, Cities in Winter and Summer. *Journal*
680 *of Geophysical Research: Atmospheres* 124, 1550–1577.
681 <https://doi.org/10.1029/2018JD029501>
- 682 Chang, Y., Huang, R., Ge, X., Huang, X., Hu, J., Duan, Y., Zou, Z., Liu, X., Lehmann,
683 M.F., 2020. Puzzling Haze Events in China During the Coronavirus (COVID-
684 19) Shutdown. *Geophys. Res. Lett.* 47. <https://doi.org/10.1029/2020GL088533>
- 685 Chen, H., Huo, J., Fu, Q., Duan, Y., Xiao, H., Chen, J., 2020. Impact of quarantine
686 measures on chemical compositions of PM_{2.5} during the COVID-19 epidemic
687 in Shanghai, China. *Science of The Total Environment* 743, 140758.
688 <https://doi.org/10.1016/j.scitotenv.2020.140758>
- 689 Chen, L., Qi, X., Nie, W., Wang, J., Xu, Zheng, Wang, T., Liu, Y., Shen, Y., Xu,
690 Zhengning, Kokkonen, T., Chi, X., Aalto, P., Paasonen, P., Kerminen, V.-M.,
691 Petäjä, T., Kulmala, M., Ding, A., 2021. Cluster Analysis of Submicron Particle
692 Number Size Distributions at the SORPES Station in the Yangtze River Delta
693 of East China. *Journal of Geophysical Research: Atmospheres* 126.
694 <https://doi.org/10.1029/2020JD034004>
- 695 Chen, L., Zhang, F., Yan, P., Wang, X., Sun, L., Li, Y., Zhang, X., Sun, Y., Li, Z., 2020.
696 The large proportion of black carbon (BC)-containing aerosols in the urban
697 atmosphere. *Environmental Pollution* 263, 114507.
698 <https://doi.org/10.1016/j.envpol.2020.114507>
- 699 Chien, L.-C., Chen, L.-W.A., Lin, R.-T., 2022. Lagged meteorological impacts on
700 COVID-19 incidence among high-risk counties in the United States—a
701 spatiotemporal analysis. *J Expo Sci Environ Epidemiol* 32, 774–781.
702 <https://doi.org/10.1038/s41370-021-00356-y>
- 703 Clemente, Á., Yubero, E., Nicolás, J.F., Caballero, S., Crespo, J., Galindo, N., 2022.
704 Changes in the concentration and composition of urban aerosols during the
705 COVID-19 lockdown. *Environmental Research* 203, 111788.
706 <https://doi.org/10.1016/j.envres.2021.111788>
- 707 Cooper, M.J., Martin, R.V., Hammer, M.S., Levelt, P.F., Veeffkind, P., Lamsal, L.N.,
708 Krotkov, N.A., Brook, J.R., McLinden, C.A., 2022. Global fine-scale changes
709 in ambient NO₂ during COVID-19 lockdowns. *Nature* 601, 380–387.



- 710 <https://doi.org/10.1038/s41586-021-04229-0>
- 711 Cui, S., Xian, J., Shen, F., Zhang, L., Deng, B., Zhang, Y., Ge, X., 2021. One-Year Real-
712 Time Measurement of Black Carbon in the Rural Area of Qingdao, Northeastern
713 China: Seasonal Variations, Meteorological Effects, and the COVID-19 Case
714 Analysis. *Atmosphere* 12, 394. <https://doi.org/10.3390/atmos12030394>
- 715 Cui, Y., Ji, D., Maenhaut, W., Gao, W., Zhang, R., Wang, Y., 2020. Levels and sources
716 of hourly PM_{2.5}-related elements during the control period of the COVID-19
717 pandemic at a rural site between Beijing and Tianjin. *Science of The Total
718 Environment* 744, 140840. <https://doi.org/10.1016/j.scitotenv.2020.140840>
- 719 Dai, Y., 2023. Data of BCc particles during the 2021 summer COVID-19 lockdown in
720 YZ. figshare. Dataset. <https://doi.org/10.6084/m9.figshare.24427795.v3>
- 721 Ding, S., Liu, D., Hu, K., Zhao, D., Tian, P., Wang, F., Li, R., Chen, Y., He, H., Huang,
722 M., Ding, D., 2021. Optical and hygroscopic properties of black carbon
723 influenced by particle microphysics at the top of the anthropogenically polluted
724 boundary layer. *Atmospheric Chemistry & Physics* 21, 681–694.
725 <https://doi.org/10.5194/acp-21-681-2021>
- 726 Feng, Z., Zheng, F., Liu, Y., Fan, X., Yan, C., Zhang, Y., Daellenbach, K.R., Bianchi, F.,
727 Petäjä, T., Kulmala, M., Bao, X., 2022. Evolution of organic carbon during
728 COVID-19 lockdown period: Possible contribution of nocturnal chemistry. *Sci
729 Total Environ* 808, 152191. <https://doi.org/10.1016/j.scitotenv.2021.152191>
- 730 Ge, B., Xu, D., Wild, O., Yao, X., Wang, J., Chen, X., Qixin, T., Pan, X., Wang, Z.,
731 2020. Inter-annual variations of wet deposition in Beijing during 2014–2017:
732 implications of below-cloud scavenging of inorganic aerosols.
733 <https://doi.org/10.5194/acp-2020-1146>
- 734 Gorelick, N., Hancher, M., Dixon, M., Ilyushchenko, S., Thau, D., Moore, R., 2017.
735 Google Earth Engine: Planetary-scale geospatial analysis for everyone. *Remote
736 Sensing of Environment, Big Remotely Sensed Data: tools, applications and
737 experiences* 202, 18–27. <https://doi.org/10.1016/j.rse.2017.06.031>
- 738 He, C., Liou, K.-N., Takano, Y., Zhang, R., Levy Zamora, M., Yang, P., Li, Q., Leung,
739 L.R., 2015. Variation of the radiative properties during black carbon aging:
740 theoretical and experimental intercomparison. *Atmospheric Chemistry and
741 Physics* 15, 11967–11980. <https://doi.org/10.5194/acp-15-11967-2015>
- 742 Hopke, P.K., Gao, N., Cheng, M.-D., 1993. Combining chemical and meteorological
743 data to infer source areas of airborne pollutants. *Chemometrics and Intelligent
744 Laboratory Systems, Proceedings of the 5th Conference on Computer
745 Applications in Analytical Chemistry (COMPANA '92)* 19, 187–199.
746 [https://doi.org/10.1016/0169-7439\(93\)80103-0](https://doi.org/10.1016/0169-7439(93)80103-0)
- 747 Huang, X., Ding, A., Gao, J., Zheng, B., Zhou, D., Qi, X., Tang, R., Wang, J., Ren, C.,
748 Nie, W., Chi, X., Xu, Z., Chen, L., Li, Y., Che, F., Pang, N., Wang, H., Tong, D.,
749 Qin, W., Cheng, W., Liu, W., Fu, Q., Liu, B., Chai, F., Davis, S.J., Zhang, Q.,
750 He, K., 2021. Enhanced secondary pollution offset reduction of primary
751 emissions during COVID-19 lockdown in China. *Natl Sci Rev* 8, nwaa137.



- 752 <https://doi.org/10.1093/nsr/nwaa137>
- 753 Isokääntä, S., Kim, P., Mikkonen, S., Kühn, T., Kokkola, H., Yli-Juuti, T., Heikkinen,
754 L., Luoma, K., Petäjä, T., Kipling, Z., Partridge, D., Virtanen, A., 2022. The
755 effect of clouds and precipitation on the aerosol concentrations and composition
756 in a boreal forest environment. *Atmospheric Chemistry and Physics* 22, 11823–
757 11843. <https://doi.org/10.5194/acp-22-11823-2022>
- 758 Jacobson, M.Z., 2002. Analysis of aerosol interactions with numerical techniques for
759 solving coagulation, nucleation, condensation, dissolution, and reversible
760 chemistry among multiple size distributions. *Journal of Geophysical Research:
761 Atmospheres* 107, AAC 2-1-AAC 2-23. <https://doi.org/10.1029/2001JD002044>
- 762 Jain, C.D., Madhavan, B.L., Singh, V., Prasad, P., Sai Krishnaveni, A., Ravi Kiran, V.,
763 Venkat Ratnam, M., 2021. Phase-wise analysis of the COVID-19 lockdown
764 impact on aerosol, radiation and trace gases and associated chemistry in a
765 tropical rural environment. *Environmental Research* 194, 110665.
766 <https://doi.org/10.1016/j.envres.2020.110665>
- 767 Jeong, C.-H., Yousif, M., Evans, G.J., 2022. Impact of the COVID-19 lockdown on the
768 chemical composition and sources of urban PM_{2.5}. *Environmental Pollution*
769 292, 118417. <https://doi.org/10.1016/j.envpol.2021.118417>
- 770 Jiang, S., Zhao, C., Fan, H., 2021. Toward Understanding the Variation of Air Quality
771 Based on a Comprehensive Analysis in Hebei Province under the Influence of
772 COVID-19 Lockdown. *Atmosphere* 12, 267.
773 <https://doi.org/10.3390/atmos12020267>
- 774 Kahnert, M., 2010. On the Discrepancy between Modeled and Measured Mass
775 Absorption Cross Sections of Light Absorbing Carbon Aerosols. *Aerosol
776 Science and Technology* 44, 453–460.
777 <https://doi.org/10.1080/02786821003733834>
- 778 Kandler, K., Schneiders, K., Ebert, M., Hartmann, M., Weinbruch, S., Prass, M.,
779 Pöhlker, C., 2018. Composition and mixing state of atmospheric aerosols
780 determined by electron microscopy: method development and application to
781 aged Saharan dust deposition in the Caribbean boundary layer. *Atmospheric
782 Chemistry and Physics* 18, 13429–13455. [https://doi.org/10.5194/acp-18-
783 13429-2018](https://doi.org/10.5194/acp-18-13429-2018)
- 784 Laughner, J.L., Neu, J.L., Schimel, D., Wennberg, P.O., Barsanti, K., Bowman, K.W.,
785 Chatterjee, A., Croes, B.E., Fitzmaurice, H.L., Henze, D.K., Kim, J., Kort, E.A.,
786 Liu, Z., Miyazaki, K., Turner, A.J., Anenberg, S., Avise, J., Cao, H., Crisp, D.,
787 de Gouw, J., Eldering, A., Fyfe, J.C., Goldberg, D.L., Gurney, K.R.,
788 Hasheminassab, S., Hopkins, F., Ivey, C.E., Jones, D.B.A., Liu, J., Lovenduski,
789 N.S., Martin, R.V., McKinley, G.A., Ott, L., Poulter, B., Ru, M., Sander, S.P.,
790 Swart, N., Yung, Y.L., Zeng, Z.-C., 2021. Societal shifts due to COVID-19
791 reveal large-scale complexities and feedbacks between atmospheric chemistry
792 and climate change. *Proc Natl Acad Sci U S A* 118, e2109481118.
793 <https://doi.org/10.1073/pnas.2109481118>



- 794 Le, T., Wang, Y., Liu, L., Yang, J., Yung, Y.L., Li, G., Seinfeld, J.H., 2020. Unexpected
795 air pollution with marked emission reductions during the COVID-19 outbreak
796 in China. *Science* 369, 702–706. <https://doi.org/10.1126/science.abb7431>
- 797 Lei, L., Zhou, W., Chen, C., He, Y., Li, Z., Sun, J., Tang, X., Fu, P., Wang, Z., Sun, Y.,
798 2021. Long-term characterization of aerosol chemistry in cold season from 2013
799 to 2020 in Beijing, China. *Environmental Pollution* 268, 115952.
800 <https://doi.org/10.1016/j.envpol.2020.115952>
- 801 Li, L., Huang, Z., Dong, J., Li, M., Gao, W., Nian, H., Fu, Z., Zhang, G., Bi, X., Cheng,
802 P., Zhou, Z., 2011. Real time bipolar time-of-flight mass spectrometer for
803 analyzing single aerosol particles. *International Journal of Mass Spectrometry*
804 303, 118–124. <https://doi.org/10.1016/j.ijms.2011.01.017>
- 805 Li, L., Li, Q., Huang, L., Wang, Q., Zhu, A., Xu, J., Liu, Ziyi, Li, H., Shi, L., Li, R.,
806 Azari, M., Wang, Y., Zhang, X., Liu, Zhiqiang, Zhu, Y., Zhang, K., Xue, S., Ooi,
807 M.C.G., Zhang, D., Chan, A., 2020. Air quality changes during the COVID-19
808 lockdown over the Yangtze River Delta Region: An insight into the impact of
809 human activity pattern changes on air pollution variation. *Science of The Total*
810 *Environment* 732, 139282. <https://doi.org/10.1016/j.scitotenv.2020.139282>
- 811 Liu, H., Pan, X., Liu, D., Liu, X., Chen, X., Tian, Y., Sun, Y., Fu, P., Wang, Z., 2019.
812 Mixing characteristics of refractory black carbon aerosols determined by a
813 tandem CPMA-SP2 system at an urban site in Beijing. *Atmospheric Chemistry*
814 *and Physics Discussions* 1–25. <https://doi.org/10.5194/acp-2019-244>
- 815 Liu, Q., Jing, B., Peng, C., Tong, S., Wang, W., Ge, M., 2016. Hygroscopicity of
816 internally mixed multi-component aerosol particles of atmospheric relevance.
817 *Atmospheric Environment* 125, 69–77.
818 <https://doi.org/10.1016/j.atmosenv.2015.11.003>
- 819 Moffet, R.C., Rödel, T.C., Kelly, S.T., Yu, X.Y., Carroll, G.T., Fast, J., Zaveri, R.A.,
820 Laskin, A., Gilles, M.K., 2013. Spectro-microscopic measurements of
821 carbonaceous aerosol aging in Central California. *Atmospheric Chemistry and*
822 *Physics* 13, 10445–10459. <https://doi.org/10.5194/acp-13-10445-2013>
- 823 Nie, D., Shen, F., Wang, J., Ma, X., Li, Z., Ge, P., Ou, Y., Jiang, Y., Chen, Meijuan,
824 Chen, Mindong, Wang, T., Ge, X., 2021. Changes of air quality and its
825 associated health and economic burden in 31 provincial capital cities in China
826 during COVID-19 pandemic. *Atmos Res* 249, 105328.
827 <https://doi.org/10.1016/j.atmosres.2020.105328>
- 828 Polissar, A.V., Hopke, P.K., Paatero, P., Kaufmann, Y.J., Hall, D.K., Bodhaine, B.A.,
829 Dutton, E.G., Harris, J.M., 1999. The aerosol at Barrow, Alaska: long-term
830 trends and source locations. *Atmospheric Environment* 33, 2441–2458.
831 [https://doi.org/10.1016/S1352-2310\(98\)00423-3](https://doi.org/10.1016/S1352-2310(98)00423-3)
- 832 Qian, J., Liao, H., Yang, Y., Li, K., Chen, L., Zhu, J., 2022. Meteorological influences
833 on daily variation and trend of summertime surface ozone over years of 2015–
834 2020: Quantification for cities in the Yangtze River Delta. *Science of The Total*
835 *Environment* 834, 155107. <https://doi.org/10.1016/j.scitotenv.2022.155107>



- 836 Qin, M., Hu, A., Mao, J., Li, X., Sheng, L., Sun, J., Li, J., Wang, X., Zhang, Y., Hu, J.,
837 2021. PM_{2.5} and O₃ relationships affected by the atmospheric oxidizing
838 capacity in the Yangtze River Delta, China. *Science of The Total Environment*
839 152268. <https://doi.org/10.1016/j.scitotenv.2021.152268>
- 840 Ramanathan, V., Carmichael, G., 2008. Global and regional climate changes due to
841 black carbon. *Nature Geoscience* 1, 221–227. <https://doi.org/10.1038/ngeo156>
- 842 Silva, P.J., Liu, D.-Y., Noble, C.A., Prather, K.A., 1999. Size and Chemical
843 Characterization of Individual Particles Resulting from Biomass Burning of
844 Local Southern California Species. *Environ. Sci. Technol.* 33, 3068–3076.
845 <https://doi.org/10.1021/es980544p>
- 846 Song, X.-H., Hopke, P.K., Fergenson, D.P., Prather, K.A., 1999. Classification of Single
847 Particles Analyzed by ATOFMS Using an Artificial Neural Network, ART-2A.
848 *Anal. Chem.* 71, 860–865. <https://doi.org/10.1021/ac9809682>
- 849 Steinfeld, J.I., 1998. Atmospheric Chemistry and Physics: From Air Pollution to
850 Climate Change. *Environment: Science and Policy for Sustainable*
851 *Development* 40, 26–26. <https://doi.org/10.1080/00139157.1999.10544295>
- 852 Sulaymon, I.D., Zhang, Yuanxun, Hopke, P.K., Hu, J., Zhang, Yang, Li, L., Mei, X.,
853 Gong, K., Shi, Z., Zhao, B., Zhao, F., 2021a. Persistent high PM_{2.5} pollution
854 driven by unfavorable meteorological conditions during the COVID-19
855 lockdown period in the Beijing-Tianjin-Hebei region, China. *Environmental*
856 *Research* 198, 111186. <https://doi.org/10.1016/j.envres.2021.111186>
- 857 Sulaymon, I.D., Zhang, Yuanxun, Hopke, P.K., Zhang, Yang, Hua, J., Mei, X., 2021b.
858 COVID-19 pandemic in Wuhan: Ambient air quality and the relationships
859 between criteria air pollutants and meteorological variables before, during, and
860 after lockdown. *Atmospheric Research* 250, 105362.
861 <https://doi.org/10.1016/j.atmosres.2020.105362>
- 862 Sun, J., Sun, Y., Xie, C., Xu, Weiqi, Chen, C., Wang, Zhe, Li, L., Du, X., Huang, F., Li,
863 Y., Li, Z., Pan, X., Ma, N., Xu, Wanyun, Fu, P., Wang, Zifa, 2022. The chemical
864 composition and mixing state of BC-containing particles and the implications
865 on light absorption enhancement. *Atmos. Chem. Phys.* 22, 7619–7630.
866 <https://doi.org/10.5194/acp-22-7619-2022>
- 867 Sun, J., Wang, Zhe, Zhou, W., Xie, C., Wu, C., Chen, C., Han, T., Wang, Q., Li, Z., Li,
868 J., Fu, P., Wang, Zifa, Sun, Y., 2021. Measurement report: Long-term changes
869 in black carbon and aerosol optical properties from 2012 to 2020 in Beijing,
870 China (preprint). *Aerosols/Field Measurements/Troposphere/Physics (physical*
871 *properties and processes)*. <https://doi.org/10.5194/acp-2021-637>
- 872 Sun, Y., Du, W., Fu, P., Wang, Q., Li, J., Ge, X., Zhang, Q., Zhu, C., Ren, L., Xu, W.,
873 Zhao, J., Han, T., Worsnop, D.R., Wang, Z., 2016. Primary and secondary
874 aerosols in Beijing in winter: sources, variations and processes. *Atmos. Chem.*
875 *Phys.*
- 876 Sun, Y., Lei, L., Zhou, W., Chen, C., He, Y., Sun, J., Li, Z., Xu, W., Wang, Q., Ji, D., Fu,
877 P., Wang, Z., Worsnop, D.R., 2020. A chemical cocktail during the COVID-19



- 878 outbreak in Beijing, China: Insights from six-year aerosol particle composition
879 measurements during the Chinese New Year holiday. *Science of The Total*
880 *Environment* 742, 140739. <https://doi.org/10.1016/j.scitotenv.2020.140739>
- 881 Ukhov, A., Mostamandi, S., Krotkov, N., Flemming, J., Da Silva, A., Li, C., Fioletov,
882 V., Mclinden, C., Anisimov, A., Alshehri, Y., Stenchikov, G., 2020. Study of
883 SO₂ pollution in the Middle East using MERRA-2, CAMS data assimilation
884 products, and high-resolution WRF-Chem simulations. *Journal of Geophysical*
885 *Research Atmospheres*. <https://doi.org/10.1029/2019JD031993>
- 886 Wang, H., Miao, Q., Shen, L., Yang, Q., Wu, Y., Wei, H., 2021. Air pollutant variations
887 in Suzhou during the 2019 novel coronavirus (COVID-19) lockdown of 2020:
888 High time-resolution measurements of aerosol chemical compositions and
889 source apportionment. *Environmental Pollution* 271, 116298.
890 <https://doi.org/10.1016/j.envpol.2020.116298>
- 891 Wang, J., Ge, X., Sonya, C., Ye, J., Lei, Y., Chen, M., Zhang, Q., 2022. Influence of
892 regional emission controls on the chemical composition, sources, and size
893 distributions of submicron aerosols: Insights from the 2014 Nanjing Youth
894 Olympic Games. *Science of The Total Environment* 807, 150869.
895 <https://doi.org/10.1016/j.scitotenv.2021.150869>
- 896 Wang, J., Liu, D., Ge, X., Wu, Y., Shen, F., Chen, M., Zhao, J., Xie, C., Wang, Q., Xu,
897 W., Zhang, J., Hu, J., Allan, J., Joshi, R., Fu, P., Coe, H., Sun, Y., 2019.
898 Characterization of black carbon-containing fine particles in Beijing during
899 wintertime. *Atmos. Chem. Phys.* 19, 447–458. <https://doi.org/10.5194/acp-19-447-2019>
- 900
- 901 Wang, Pengfei, Chen, K., Zhu, S., Wang, Peng, Zhang, H., 2020. Severe air pollution
902 events not avoided by reduced anthropogenic activities during COVID-19
903 outbreak. *Resources, Conservation and Recycling* 158, 104814.
904 <https://doi.org/10.1016/j.resconrec.2020.104814>
- 905 Wang, S., Zhao, M., Xing, J., Wu, Y., Zhou, Y., Lei, Y., He, K., Fu, L., Hao, J., 2010.
906 Quantifying the Air Pollutants Emission Reduction during the 2008 Olympic
907 Games in Beijing. *Environ. Sci. Technol.* 44, 2490–2496.
908 <https://doi.org/10.1021/es9028167>
- 909 Wang, Y., Zhu, S., Ma, J., Shen, J., Wang, Pengfei, Wang, Peng, Zhang, H., 2021.
910 Enhanced atmospheric oxidation capacity and associated ozone increases
911 during COVID-19 lockdown in the Yangtze River Delta. *Science of The Total*
912 *Environment* 768, 144796. <https://doi.org/10.1016/j.scitotenv.2020.144796>
- 913 Wang, Y.Q., 2014. MeteoInfo: GIS software for meteorological data visualization and
914 analysis. *Meteorological Applications* 21, 360–368.
915 <https://doi.org/10.1002/met.1345>
- 916 Wang, Y.Q., Zhang, X.Y., Draxler, R.R., 2009. TrajStat: GIS-based software that uses
917 various trajectory statistical analysis methods to identify potential sources from
918 long-term air pollution measurement data. *Environmental Modelling &*
919 *Software* 24, 938–939. <https://doi.org/10.1016/j.envsoft.2009.01.004>



- 920 WHO global air quality guidelines: Particulate matter (PM_{2.5} and PM₁₀), ozone,
921 nitrogen dioxide, sulfur dioxide and carbon monoxide, 2021. , WHO Guidelines
922 Approved by the Guidelines Review Committee. World Health Organization,
923 Geneva.
- 924 Xie, C., He, Y., Lei, L., Zhou, W., Liu, J., Wang, Q., Xu, W., Qiu, Y., Zhao, J., Sun, J.,
925 Li, L., Li, M., Zhou, Z., Fu, P., Wang, Z., Sun, Y., 2020. Contrasting mixing
926 state of black carbon-containing particles in summer and winter in Beijing.
927 *Environmental Pollution* 263, 114455.
928 <https://doi.org/10.1016/j.envpol.2020.114455>
- 929 Xu, J., Ge, X., Zhang, X., Zhao, W., Zhang, R., Zhang, Y., 2020. COVID-19 Impact on
930 the Concentration and Composition of Submicron Particulate Matter in a
931 Typical City of Northwest China. *Geophysical Research Letters* 47,
932 e2020GL089035. <https://doi.org/10.1029/2020GL089035>
- 933 Yang, J., Ma, S., Gao, B., Li, X., Zhang, Y., Cai, J., Li, M., Yao, L., Huang, B., Zheng,
934 M., 2017. Single particle mass spectral signatures from vehicle exhaust particles
935 and the source apportionment of on-line PM_{2.5} by single particle aerosol mass
936 spectrometry. *Science of The Total Environment* 593–594, 310–318.
937 <https://doi.org/10.1016/j.scitotenv.2017.03.099>
- 938 Zhang, F., Wang, Yuan, Peng, J., Chen, L., Sun, Y., Duan, L., Ge, X., Li, Y., Zhao, J.,
939 Liu, C., Zhang, X., Zhang, G., Pan, Y., Wang, Yuesi, Zhang, A.L., Ji, Y., Wang,
940 G., Hu, M., Molina, M.J., Zhang, R., 2020. An unexpected catalyst dominates
941 formation and radiative forcing of regional haze. *Proceedings of the National
942 Academy of Sciences* 117, 3960–3966.
943 <https://doi.org/10.1073/pnas.1919343117>
- 944 Zhang, G., Fu, Y., Peng, X., Sun, W., Shi, Z., Song, W., Hu, W., Chen, D., Lian, X., Li,
945 L., Tang, M., Wang, X., Bi, X., 2021. Black Carbon Involved Photochemistry
946 Enhances the Formation of Sulfate in the Ambient Atmosphere: Evidence From
947 In Situ Individual Particle Investigation. *Geophys Res Atmos* 126.
948 <https://doi.org/10.1029/2021JD035226>
- 949 Zhang, J., Li, H., Chen, L., Huang, X., Zhang, W., Zhao, R., 2022. Particle composition,
950 sources and evolution during the COVID-19 lockdown period in Chengdu,
951 southwest China: Insights from single particle aerosol mass spectrometer data.
952 *Atmospheric Environment* 268, 118844.
953 <https://doi.org/10.1016/j.atmosenv.2021.118844>
- 954 Zhang, J., Yuan, Q., Liu, L., Wang, Y., Zhang, Y., Xu, L., Pang, Y., Zhu, Y., Niu, H.,
955 Shao, L., Yang, S., Liu, H., Pan, X., Shi, Z., Hu, M., Fu, P., Li, W., 2021. Trans-
956 Regional Transport of Haze Particles From the North China Plain to Yangtze
957 River Delta During Winter. *JGR Atmospheres* 126.
958 <https://doi.org/10.1029/2020JD033778>
- 959 Zhang, K., Liu, Z., Zhang, X., Li, Q., Jensen, A., Tan, W., Huang, L., Wang, Y., de Gouw,
960 J., Li, L., 2022. Insights into the significant increase in ozone during COVID-
961 19 in a typical urban city of China. *Atmos. Chem. Phys.* 22, 4853–4866.



- 962 <https://doi.org/10.5194/acp-22-4853-2022>
- 963 Zhang, Y., Liu, X., Zhang, L., Tang, A., Goulding, K., Collett, J.L., 2021. Evolution of
964 secondary inorganic aerosols amidst improving PM_{2.5} air quality in the North
965 China plain. *Environmental Pollution* 281, 117027.
966 <https://doi.org/10.1016/j.envpol.2021.117027>
- 967 Zhang Y., Wang X., Chen H., Yang X., Chen J., Alien J.O., 2009. Source Apportionment
968 Of Lead-containing Aerosol Particles In Shanghai Using Single Particle Mass
969 Spectrometry. *Chemosphere* 74, 501–507.
- 970 Zhang, Y., Yuan, Q., Huang, D., Kong, S., Zhang, J., Wang, X., Lu, C., Shi, Z., Zhang,
971 X., Sun, Y., Wang, Z., Shao, L., Zhu, J., Li, W., 2018. Direct Observations of
972 Fine Primary Particles From Residential Coal Burning: Insights Into Their
973 Morphology, Composition, and Hygroscopicity. *Journal of Geophysical
974 Research: Atmospheres* 123, 12,964-12,979.
975 <https://doi.org/10.1029/2018JD028988>
- 976 Zhou, H., Liu, T., Sun, B., Tian, Y., Zhou, X., Hao, F., Chun, X., Wan, Z., Liu, P., Wang,
977 J., Du, D., 2022. Chemical characteristics and sources of PM_{2.5} in Hohhot, a
978 semi-arid city in northern China: insight from the COVID-19 lockdown. *Atmos.
979 Chem. Phys.* 14.
- 980 Zhou, Y., Wu, Y., Yang, L., Fu, L., He, K., Wang, S., Hao, J., Chen, J., Li, C., 2010. The
981 impact of transportation control measures on emission reductions during the
982 2008 Olympic Games in Beijing, China. *Atmospheric Environment* 44, 285–
983 293. <https://doi.org/10.1016/j.atmosenv.2009.10.040>
- 984 Zhu, X., Hu, B., Xin, J., Wang, L., Münkel, C., Mao, G., Wang, Y., 2015. Impact of
985 emission controls on air quality in Beijing during APEC 2014: Lidar ceilometer
986 observations. *ATMOSPHERIC CHEMISTRY AND PHYSICS* 15, 12667–
987 12680. <https://doi.org/10.5194/acp-15-12667-2015>
- 988
- 989
- 990